Wavelength-Selective Nonlinear Imaging and Photo-Induced Cell Damage by Dielectric Harmonic Nanoparticles

Kilin, Vasyl; Campargue, Gabriel; Fureraj, Ina; Sakong, Sim; Sabri, Tarek; Riporto, Florian; Vieren, Alice; Mugnier, Yannick; Mas, Christophe; Staedler, Davide; Collins, John Michael; Bonacina, Luigi; Vogel, Alfred; Capobianco, John A. [**and 1 more**]

Article

Wavelength-Selective Nonlinear Imaging and Photo-Induced Cell Damage by Dielectric Harmonic Nanoparticles

Vasyl Kilin, Gabriel Campargue, Ina Fureraj, Sim Sakong, Tarek Sabri, Florian Riporto, Alice Vieren, Yannick Mugnier, Christophe Mas, Davide Staedler, John Michael Collins, Luigi Bonacina, Alfred Vogel, John A. Capobianco, and Jean-Pierre Wolf

ACS Nano, **Just Accepted Manuscript** • DOI: 10.1021/acsnano.9b08813 • Publication Date (Web): 13 Apr 2020

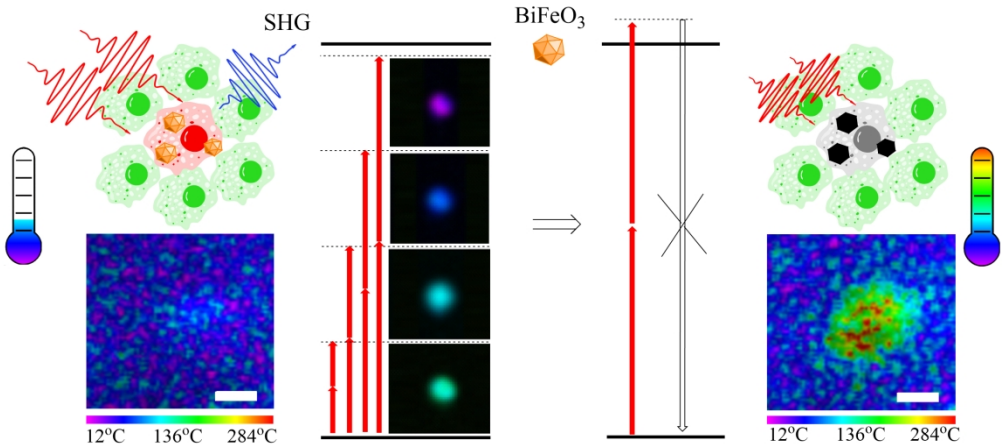

TOC for manuscript

672x298mm (96 x 96 DPI)

Wavelength-Selective Nonlinear Imaging and Photo-Induced Cell Damage by Dielectric Harmonic Nanoparticles

Vasyl Kilin,[*,†] Gabriel Campargue,[†] Ina Fureraj,[†] Sim Sakong,[†] Tarek Sabri,[‡] Florian Riporto,[¶] Alice Vieren,[†] Yannick Mugnier,[¶] Christophe Mas,[§] Davide Staedler,[‖] John Michael Collins,[⊥] Luigi Bonacina,[†] Alfred Vogel,[#] John A. Capobianco,[‡] and Jean-Pierre Wolf[†]

†*Department of Applied Physics, Université de Genève, 22 chemin de Pinchat, 1211 Genève 4, Switzerland*

‡*Department of Chemistry and Biochemistry and Centre for NanoScience Research, Concordia University, 7141 Sherbrooke St. West, Montreal, Canada*

¶*Univ. Savoie Mont Blanc, SYMME, F-74000 Annecy, France*

§*OncoTheis Sàrl, 18 chemin des Aulx, CH-1228, Plan-les-Ouates, Geneva, Switzerland*

‖*Department of Pharmacology and Toxicology, University of Lausanne, Lausanne, Switzerland*

⊥*Wheaton College, 26 E. Main Street Norton, MA 02766, United States of America*

#*Institute of Biomedical Optics University of Luebeck, Peter-Monnik-Weg 4, 23562 Luebeck, Germany*

E-mail: vasyl.kilin@unige.ch

Abstract

We introduce a nonlinear all-optical theranostics protocol based on the excitation wavelength decoupling between imaging and photo-induced damage of human cancer cells labelled by Bismuth Ferrite (BFO) harmonic nanoparticles (HNPs). To characterize the damage process, we rely on a scheme for *In Situ* temperature monitoring based on upconversion nanoparticles: by spectrally resolving the emission of silica coated NaGdF4: Yb^{3+}/Er^{3+} nanoparticles in close vicinity of a BFO HNP, we show that the photo-interaction upon NIR-I excitation at high irradiance is associated with a temperature increase $> 100°$ C. The observed laser-cell interaction implies a permanent change of the BFO nonlinear optical properties which can be used as a proxy to read-out the outcome of a theranostics procedure combining imaging at 980 nm and selective cell damage at 830 nm. The approach has potential applications to monitor and treat lesions within NIR light penetration depth in tissues.

Keywords

photo-induced cell damage; harmonic generation; harmonic nanoparticles; upconversion nanoparticles; nanothermometry

Nanoparticle-based theranostics is often associated with multimodal interaction in which the control over diagnostics (imaging) and treatment (*e.g.*, cell disruption, drug-release) procedures is exerted by physically distinct stimuli (*e.g.*, optical, magnetic). In some settings, the rapid access to different kinds of interaction exploiting the same physical vector and equipment can be the key to success. Approaches based on plasmonic absorption of gold nanoparticles have been intensively studied in the last decade.[1] In this case, irradiation at low pulse-energy enables the use of nanoparticles as markers, whereas an increasing of pulse energy results in thermomechanical effects that can be used for localized destruction of target cells or structures. However, from the practical viewpoint, the separation

between the two regimes is difficult to control, especially when thick cell layers are irradiated and the radiant exposure changes as a function of depth. In this work, we investigate the excitation-wavelength decoupling between imaging and photo-induced damage of cells labelled by Bismuth Ferrite (BFO) harmonic nanoparticles (HNPs). It was previously shown that BFO HNPs are suitable cell markers for nonlinear microscopy.[2,3] Their contrast is based on second- and third-harmonic generation (SHG, THG) rather than luminescence. Harmonic generation is a parametric nonlinear process where N incident photons at frequency ω interacting with a nonlinear medium are scattered as a single photon at frequency $N \times \omega$. As we previously demonstrated, the co-localization of SHG and THG typically excited between 1200-1300 nm leads to additional selectivity against background, in fact it can be exploited to detect HNP-labelled structures against endogenous sources of harmonic signals,[2,3] such as collagen or lipids.[4] Furthermore, the long excitation wavelengths strongly limit autofluorescence that may hinder the marker detection in tissues.

The procedure we demonstrate here implies harmonic generation using excitation $\geq$980 nm for imaging, followed by photo-interaction at shorter wavelengths (820-830 nm) for localized damage of BFO labelled cells. Although the process of harmonic generation is not directly associated with photon absorption, it is known, that nonlinear conversion efficiency can be enhanced when the excitation or emission frequency is tuned to a resonance.[5] In this case, concomitant with the harmonic emission, heat can be deposited onto the particle following direct multiphoton excitation or linear re-absorption of SHG.[6] Within this resonant approach, the temperature reached by a ZnO nanowire excited by two-photon above the band gap frequency was recently estimated to 327° C.[7] The amount of temperature increase does not exclusively rely on the choice of the excitation frequency, but also on other parameters playing a role in local heating dynamics, in particular the numerical aperture (NA) of the focused beam,[8] the laser repetition rate, and the dwell time.[8,9] Keeping all other conditions identical, MHz sources are more effective for heating than kHz ones because the inter-pulse delay is short compared to heat dissipation rate.

To demonstrate the possibility to select the photo-interaction modality by wavelength-switching, we characterize the process in three stages. i) We study the dependence of imaging and permanent damage as a function of peak irradiance, irradiation dose, and wavelength for BFO HNPs, unlabelled and labelled cancer cells. ii) We devise an all-optical scheme based on NaGdF4: Yb^{3+}/Er^{3+} upconversion nanoparticles for *In Situ* temperature monitoring around a nanometric heating source. iii) We demonstrate the spatial selectivity of the photo-damage procedure on a co-culture containing labelled and unlabelled cells.

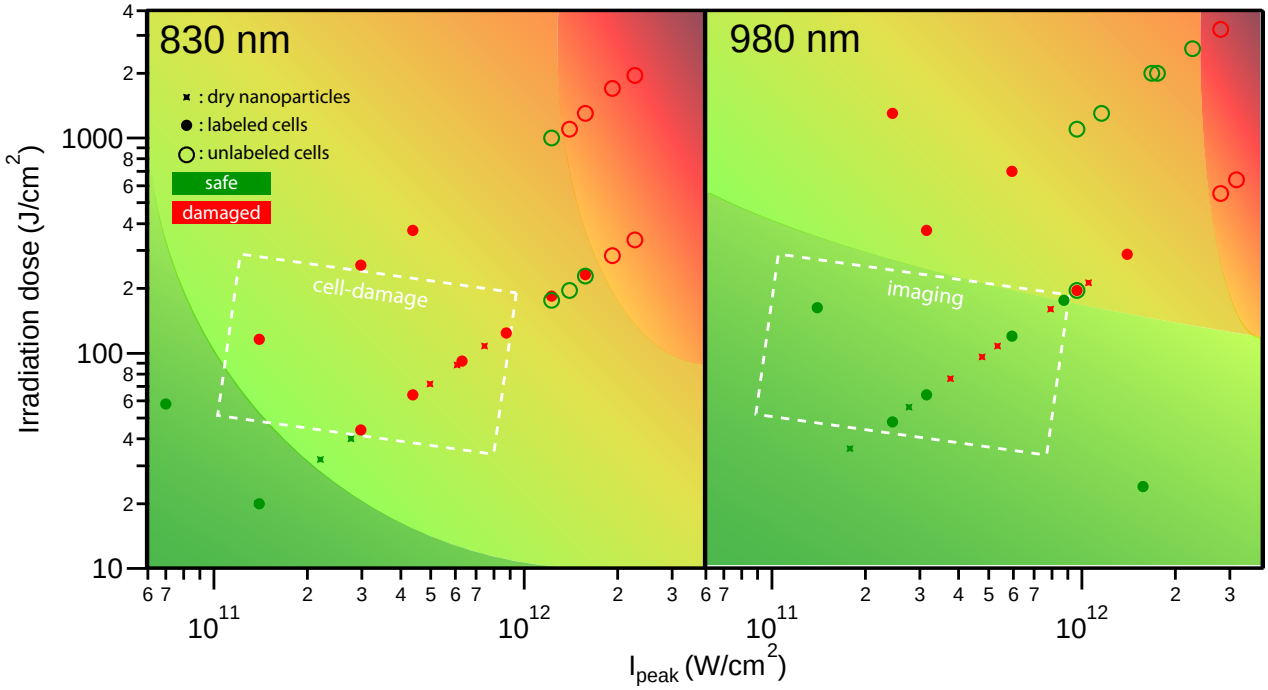

Figure 1: Assesement of photo-induced damage as a function of irradiance and irradiation dose on dry BFO HNPs dispersed on a microscope coverslip (stars), unlabelled A549 cells (open circles), and BFO-labelled A549 cells (filled circles). Green corresponds to safe exposure and red to unsafe exposure observed during the first image scan as detailed in the Materials and Methods section. Variation of irradiance goes along with a variation of the total irradiation dose that depends on pixel dwell time (4.1 μs and 23,8 μs for the measurements in the lower and upper diagonal series, respectively). The dashed box outlines the theranostics window, *i.e.* an irradiance/irradiation dose region characterized by a different interaction modality (imaging, photo-damage) on labelled cells when the wavelength is switched between 980 nm to 830 nm.

Results and Discussion

Figure 1 provides an overview of the photo-induced effects of different irradiation parameters. Damage thresholds for dry particles or small particle aggregates, labelled cells, and unlabelled cells exhibit pronounced differences at 830 and 980 nm. This makes it possible to identify parameter regimes for damage-free cell imaging at 980 nm, and targeted cell destruction at 830 nm (see dashed boxes). These regimes and the underlying interaction mechanisms will now be discussed in details.

Effect of Laser Irradiation on Dry BFO HNPs on a Substrate

The direct band-gap of BFO is approximately centered at 450 nm (2.7 eV).[10] Upon resonant interaction in this spectral region, differently from what has been reported for ZnO,[5,6,11] for two-photon excitation $>$ 800 nm we observe pristine SHG spectra and no or very weak photo-luminescence (Fig. S.I. 2, upper plot). The latter is normally reported for one-photon excitation $<$400 nm.[12] On the other hand, we observe that the SHG signal vanishes permanently upon irradiation at intensities and irradiation doses above specific threshold values (Fig. 1). As reported in Fig. S.I.3, the dynamics of the SHG signal from a large ensemble of BFO HNPs on a substrate undergoing areal scanning irradiation follows a characteristic decay. The sudden drop at the beginning of the irradiation procedure originates from the complete loss of SHG from the larger HNP aggregates present on the substrate with concomitant emission of a broadband luminescence signal (Fig. S.I.2, lower plot). The slower decay stems from the progressive disappearance of SHG from smaller aggregates and isolated nanoparticles.

The SHG loss is likely associated with processes affecting the noncentrosymmetric crystal structure of BFO.[13] The XRD pattern measured for BFO HNP powder irradiated at high

peak irradiance at 820 nm for several consecutive hours present several distinct features as compared to the traces obtained for samples treated at low irradiation or not irradiated (Fig. S.I.5). In particular, the highly irradiated sample trace indicates the presence of SHG-inactive phases such as metal Bi and Fe_3O_4. This finding is likely related to a major rise in the local temperature, but it also points to a reduction of the oxidation state of the Bi^{3+} and Fe^{3+} ions. Previous work on the temperature dependence of the crystal structure already enables a rough assessment of the temperature rise associated with the structure modifications observed in the present study. In the 447°C-767°C range, bulk BFO is known to be less thermodynamically stable than the sillenite $Bi_{25}FeO_{39}$ and $Bi_2Fe_4O_9$ phases.[14] The irreversible transformation of sol-gel BFO powders to $Bi_2Fe_4O_9$ above 504°C has also been reported.[15] In the case of nanoparticles, these temperature values should be taken as indicative, because of very probable size-effects. Decomposition by-products with different absorption properties might also contribute to local heating by changes in the optical absorptivity upon irradiation, as previously observed in the ablation of dielectric materials.[16,17]

In Fig. 1, star symbols indicate all the irradiation conditions tested on dry BFO HNPs as a function of peak irradiance, irradiation dose, and wavelength (left: 830 nm, right: 980 nm). The first two parameters are calculated according to the expressions reported in Materials and Methods. The irradiation dose is computed considering exclusively a single image frame. Consequently, we report in red the datapoints corresponding to exposure settings leading to the observation of nanoparticles' SHG suddenly disappearing during the first image scan concomitant with the emission of luminescence, while the irradiation-safe conditions are indicated in green.

Temperature Rise Around BFO HNPs

To calculate the extent of the temperature rise associated with the damage onset, we developed a specific protocol to image and quantify *In Situ* the temperature increase of nanopar-

ticles upon laser irradiation. We used 30 nm silica-coated $NaGdF_4$: Yb^{3+}/Er^{3+} upconverting nanoparticles (UCNPs) as local temperature probes by exploiting the thermal sensitivity of the $^2H_{11/2}$ and $^4S_{3/2} \rightarrow ^4I_{15/2}$ emissions of the Er^{3+} ion. The temperature can be estimated by measuring the ratio of the two fluorescence intensities centered at 525 and 545 nm.[18] This spatially resolved approach provides access to the heterogeneity of HNP individual responses. Similar procedures have already been developed with different upconversion nanomaterials in other settings, for example by heating gold nano rods embedded in a biological tissue and using CaF_2:Nd^{3+},Y^{3+} for ratiometric temperature read-out.[19]

As illustrated in Fig. 2a, we prepared a sample by casting a drop of a mixture of BFO HNPs and UCNPs on a glass coverslip and letting the solvent evaporate. We successively acquired an image with the laser tuned to 980 nm under HNP-safe settings. The hyperspectral images obtained under these conditions are shown in Figs. 2b and 2c. The former plot is limited to the spectral channels in the SHG region (480-515 nm), the latter covers the full spectral range, 480-565 nm (Fig. 2c). The images indicate the presence of a small HNP nanoparticle aggregate emitting a strong SHG signal superposed to a homogeneous layer of UCNP emission. Figure 2d shows the characteristic UCNP emission spectrum featuring the two bands in the visible region upon NIR excitation. These green bands can be conveniently separated from the narrow SHG blue emission at 490 nm when UCNPs and BFO HNPs are simultaneously excited at 980 nm. We calibrated the response of UCNPs under our imaging conditions (without HNPs) by artificially changing the temperature of the substrate where the UCNPs are deposited using a home-built Peltier element slide holder. The band intensity ratio was fitted according to $I_{525}/I_{540} = C \exp \Delta E/kT$, with C being an experimental constant, k the Boltzmann constant, and ΔE the energy difference among the excited states of the Er^{3+} ion leading to the I_{525} and I_{540} bands.[18] Notably, the agreement of the data points to the fitting function is preserved throughout the entire investigated temperature range, 30-120°C.

For visualizing the temperature distribution around BFO HNPs, the area shown in panels

b and c was irradiated under excitation conditions below and above threshold for photo-damage of BFO dry nanoparticles. Note that for this specific measurement, we set the laser at 980 nm for photo-damage in order to collect SHG and also resonantly trigger the upconversion process. From the analysis of the UCNP I_{525}/I_{540} ratio, we found that this exposure entails a significant temperature rise, up to >200°C for some HNPs. This value was extrapolated from the fit to the experimentally determined calibration curve measured up to 120° C (Fig. 2d). The temperature-resolved maps in Figs. 2e and 2f at low and high irradiance/dose settings, respectively, indicate that the temperature increase colocalizes with the position of the SHG-active particle.

Figure 3 shows the kinetics of the SHG loss under the same irradiation conditions as in Fig. 2d and 2f and the concomitant temperature rise. The kinetic traces in Fig. 3a were obtained by averaging the response of a few (N =3) HNPs. We repeated the procedure on a larger number of particles (N =25) in order to define a statistical distribution of the temperature increase (Fig. 3b). HNPs are heating up to 100°C on average, with a fairly broad distribution indicating a large particle-to-particle variability, which might be associated with the aggregation state or the size, according to the broad distribution measured by DLS (see Fig. S.I. 1).[20] We assume that the actual temperature is even higher than 100° C considering that we detect time-averaged values at a slow frame rate (0.25 frame per second, fps).

BFO HNP-Mediated Cell Damage

After having assessed the photo-damage on the dry particles at two selected wavelengths, we now study the effect of BFO HNP-mediated light-interaction in cell medium and on living cells. In Fig. S.I.4, we report the results of the protocol described for dry NPs applied to BFO HNPs in cell medium. The outcome of the measurement is quantitatively similar, displaying a slightly lower temperature increment consistent with the different thermal properties of the surrounding medium. For this temperature estimation, we applied the calibration of Fig.2.

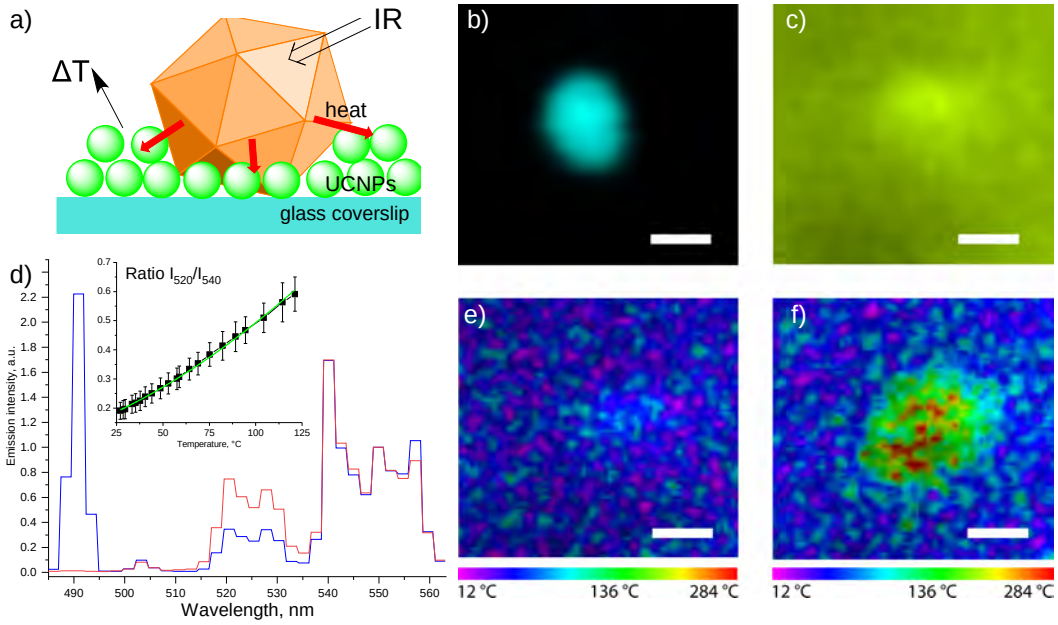

Figure 2: *In Situ*characterization of the temperature increase around a small BFO particle aggregate probed by UCNPs nanothermometry. **a)** Schematic representation of the sample. **b** and **c)** Hyperspectral images of a BFO particle surrounded by UCNPs excited at 980 nm. The SHG emission centered at 490 nm is visible in the 485-515 nm spectral region (b). UCNPs luminescence overlaps the SHG emission when the full 485-565 nm spectral range is shown (c). **d)** Spectrally resolved emission of a HNP and UCNP mixture as in a) obtained with irradiance/irradiation dose below (blue line, showing the SHG peak at 490 nm) and above threshold with loss of SHG (red line). The traces are normalized by the emission intensity at 540 nm. Inset: Temperature calibration curve showing the UCNP I_{520}/I_{540} intensity ratio as a function of the substrate temperature. **e)** and **f)** Temperature-resolved images of the particle in panels b) and c) plotted using a false-color map extracted from the calibration curve in d). The excitation intensity corresponds to the photostable regime (b, c and e) and permanent loss of SHG (f), respectively. Scale bar 1 μm.

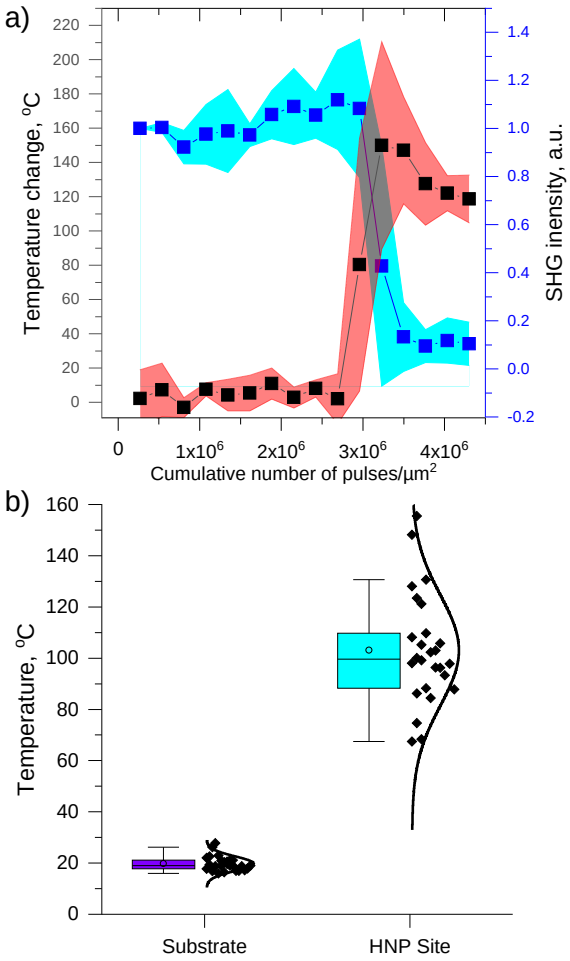

Figure 3: **a)** Time evolution of the temperature change (red) and SHG intensity (blue) during irradiation. Each data point corresponds to an image of a sequence acquired at 0.25 fps.**b)** Temperature distribution in the absence (left, *Substrate*) and in close proximity (right, *HNP Site*) of a BFO HNP.

Although an approximate, this approach is partially justified by the findings of Balabhadra *et al.* who showed that the thermal calibration is only slightly dependent on the surrounding medium.[21] Quintanilla *et al.* have shown that this dependence can be associated with the light extinction properties of the UCNP environment. Indeed, absorption and scattering in the sample might differ at the wavelengths of the two emission bands used for the ratiometric temperature estimation.[19] This effect was recently observed in experiments on 3D cell cultures treated with different media.[22] The epi-detection configuration of our set-up should minimize this effect, in fact by collecting the backward emission we ensure that upconverted photons travel through a very thin sample layer.

An increase in autofluorescence intensity correlated with cell damage upon laser irradiation has been reported by several authors[23,24] and it is commonly referred to as hyperfluorescence.[25] By monitoring the onset of strong hyperfluorescent spots, we first determined the intensity required for direct cell damage by irradiating adenocarcinomic human alveolar epithelial cells (A549) without nanoparticles. For this procedure we used red fluorescent protein (RFP) expressing cells. The irradiation conditions tested for 830 and 980 nm excitation are reported in Fig. 1. Unlabeled cells (open circles) appear in green when we observed no visible damage upon laser exposure, and in red when they are affected. The position of the boundaries between the two possible outcomes in the plots is wavelength-dependent, as already reported.[26] We colored in red the region of irradiation parameters unsafe for unlabelled cells and in green the region that is safe for both unlabelled and labelled cells (the shaded areas in the plots are exclusively based on the data points reported, and should be considered qualitative guidelines to ease the inspection of the plots).

Similarly, labelled cells are indicated as green and red filled circles, for safe and unsafe irradiation conditions, respectively. As compared to the case of unlabelled cells, the presence of BFO HNPs clearly shifts the threshold leading to photo-damage to lower irradiance/dose values. In case of very sparsely labelled cells (containing only a few HNPs, not shown), photo-damage takes place at higher irradiance/irradiation dose values. We also notice that dry

HNPs have the tendency to be photo-damaged at lower irradiation parameters than labelled cells, likely because of the absence of a water environment facilitating heat dissipation.

Overall, we can now delineate three distinct regions for the interaction: i) the green region corresponds to conditions not leading to the observation of hyperfluorescent spots in labelled cells; ii) the yellow region characterizes laser exposure settings affecting labelled cells while preserving unlabelled cells; and, finally, iii) the red region is associated with damage both for labelled and unlabelled cells. The parameters characterizing these regions are critically sensitive to the wavelength used for the excitation. The comparison between 830 and 980 nm plots allows defining an interaction area (dashed white square), where a different outcome on cells is expected depending only on wavelength change while maintaining identical the irradiance/dose values. The existence of this region demonstrates the possibility to follow a theranostics approach based on switching the interaction modality with laser wavelength. Note that, instead of working exclusively in NIR-I, one can follow the same approach and take full advantage of NIR-II for imaging as this spectral region can be easily accessed using HNPs.[2]

To mimic a situation where the laser treatment at 830 nm should selectively target a cell sub-population preserving non-labelled ones and maintaining single-cell resolution, we plated in a glass-bottom Petri dish a co-culture containing both wild-type and BFO-preloaded cells. This scenario is illustrated in Fig. S.I.3. The cell at the center of the field of view displays a strong SHG-active area, associated with BFO HNP internalization and aggregation. After laser treatment, intracellular regions which were initially SHG-active start exhibiting a bright and spectrally broad hyperfluorescence emission.

In Fig. 4, we show the evolution of the laser-induced BFO HNP-mediated cell modifications and its high spatial selectivity. During the treatment, performed on a surface of 150×150 μm^2 centered on a BFO labelled cell, a strongly luminescent area develops. It is initially confined in a few isolated spots and eventually covers a large fraction of the cell body. Figure 5 presents a quantitative analysis of the spectral changes in luminescence and SHG

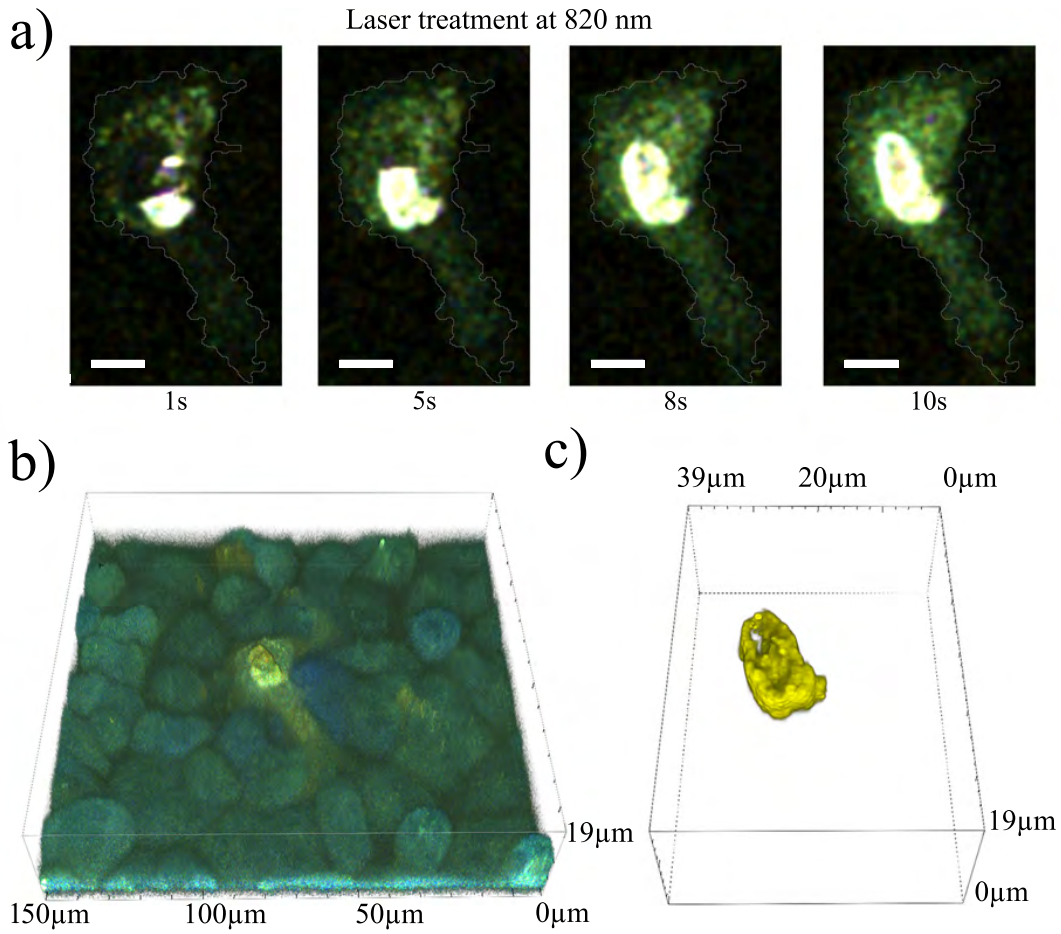

Figure 4: **a)** Evolution of hyperfluorescence during the laser treatment. **b)** Three-dimensional reconstruction of a co-culture containing BFO-labelled and unlabelled cells exposed to irradiation at 820 nm. The reconstruction was obtained by autofluorescence imaging *via* two-photon excitation at 720 nm. Note the presence of a damaged cell in the center. **c)** Identification of the laser-ablated region obtained by spectrally unmixing the emission signal. As a reference for unmixing, the emission spectrum of ablated cells reported in Fig. 5a is used.

emission going along with cell damage and the time-evolution of SHG and hyperfluorescence signals. Spectrally, we observe a clear red-shift from autofluorescence to hyperfluorescence (Fig. 5a). This feature is consistent with the spectra reported by Qu's group in a series of recent works on femtosecond laser surgery.[27,28] As shown in Fig. 5b, hyperfluorescence sets in upon the loss of SHG, which is indicative for a temperature rise $> 80°$ (Fig. 3a). Interestingly, Hovhannisyan *et al.* have also described a similar signal kinetics with a clear temporal correlation between the loss of SHG from collagen fibers irradiated by a femtosecond laser and the appereance of hyperfluorescence, and attributed it to free-electron mediated damage.[29]

After the treatment, we acquired a volume image of the whole irradiated region by autofluorescence (Fig. 4b). We observe that the unlabelled cells surrounding the target cell are not visibly affected by the laser irradiation. By applying a spectral-deconvolution procedure to isolate the image regions associated with the characteristic hyperfluorescence of damaged cells (orange trace in Fig. 5a), we were able to precisely delineate the photo-interaction volume (Fig. 4c). Its interior is not fluorescent, suggesting either material ablation or, alternatively, a complete bleaching of the fluorescing/hyperfluorescing species. The former scenario is compatible with the expansion of a thermally generated cavitation bubble as previously reported for direct femtosecond laser ablation.[8]

Our results demonstrate the exsistence of distinct parameter regions for damage-free SHG image of BFO labelled cells and selective modifications. The photo-induced damage remains confined within HNP-labelled cells and preserves neighboring structures, because of the difference in the damage threshold among BFO HNPs and unlabelled cells (Fig. 1). The mechanism of cell damage relies on different effects. Under the irradiation conditions we explored, nonlinear photochemistry and free-electrons mediated effects play a major role in cellular modifications.[8,30] On the other hand, the interaction is associated with a rise of the local temperature around the HNP. By the UCNPs-based protocol (Fig. 2 and 3), we have demonstrated that the temperature increase in the immediate vicinity of a photo-excited BFO HNP can easily exceed 100° C. This temperature rise, although essential to the pro-

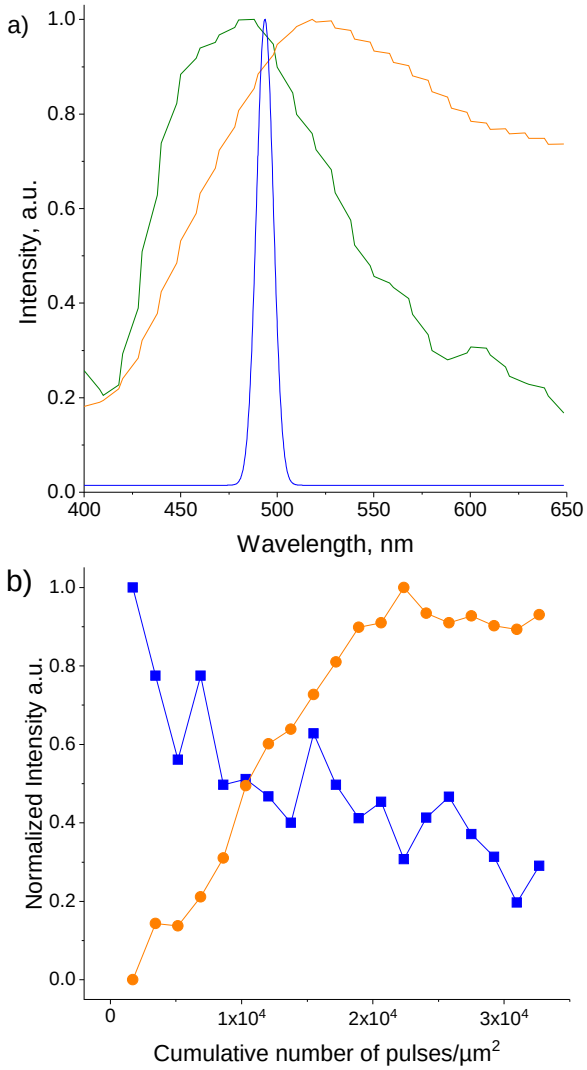

Figure 5: **a)** Normalized emission spectra of a selected cell before (green) and after (orange) laser treatment along with the SHG emission spectrum (cyan). **b)** Time evolution of SHG (blue) and hyperfluorescence (orange) intensity from a laser-damaged region within the cell.

cess, is not the unique element of the disruption mechanism. Thermal denaturation cannot play a leading role at the short heat exposure times (microsecond dwell times) to which the cells are exposed:[31] the temperature needed to produce photo-denaturation within microseconds is higher than the threshold for explosive vaporization.[32] The cell damage produced by BFO HNPs is most likely a mixture of thermomechanical effects and free-electron-mediated molecular modifications. This scenario is corroborated by the observation of the cavity in Fig. 4c, which can arise either from vaporization of tissue water at the heterogeneous nucleation threshold (at the HNP/cytoplasma interface), or from disintegration of biomolecules into noncondensable gas *via* nonlinear chemistry or free-electron-mediated bond breaking.

Conclusions

Use of optical probes such as BFO HNPs combined with different irradiation parameters could enable theranostics applications. The inherent nonlinear dependence of the photo-interaction by BFO HNPs exploited in this work leads to the efficient wavelength decoupling between imaging at 980 nm and photo-interaction at 830 nm and confines the instantaneous interaction to a very small focal volume which can be displaced in three dimensions. As a drawback, nonlinear excitation requires comparatively higher intensities than linear photothermal methods[33] and relies on raster-scanning rather than large area irradiation. Conveniently, the wavelengths needed for our approach can be selected in the first and second transmission windows of biological tissues (NIR-I: 650-950 nm, and NIR-II: 1100-1350 nm), which entails optimal conditions in terms of optical penetration depth.[34] Thanks to recent progresses in femtosecond laser technologies, nowadays the whole 700-1300 nm range can be covered by a single tunable source, enabling a rapid switching between the two interaction modalities.

The temperature rise that we were able to characterize by using $NaGdF_4$: Yb^{3+}/Er^{3+} UCNPs together with free-electrons mediated effects lead to a complete loss of SHG emis-

sion, which can be used as a real-time optical read-out of the success of the photo-interaction and may be amenable to achieve homogeneous effects through relatively thick target layers. Based on all these considerations, we believe that cell disruption in conjunction with BFO HNPs could be an enabling theranostic tool in medical procedures such as margin resection and clean up after cancer surgery[35] because of the complete and highly selective disruption of labelled cells and the immediate read-out of the success of the procedure associated with the sudden disappear of narrow-banded SHG emission by HNPs upon laser-induced decomposition. To overcome constraints given by the limited optical penetration depth of biological tissues, the technique could, for *In Vivo* applications inside the bodya, be implemented in a nonlinear endoscopy set-up.[36]

Materials and Methods

BFO Nanoparticles BFO nanoparticles provided by the company FEE GmbH (Idar-Oberstein, Germany) were obtained as ethanol stabilized colloidal suspensions. As reported earlier,[20] the synthesis is based on the auto-combustion method with Bi and Fe nitrate salts firstly dissolved in an acidic solution. After addition of a fuel, namely 2-amino-2-hydroxymethyl-propane-1,3-diol, and drying at 105° C, the obtained dried resin ignites itself leading to BFO powders showing secondary phases of different oxides. Phase purity is then improved by a 1 hour calcination step at 600° C. Because of the auto-ignition procedure, this scalable approach results in batch-to-batch variation in terms of residual impurities and the absence of size and shape control for the HNPs.[20] Stable suspensions of BFO are, however, readily obtained after wet milling of the calcined powder on a rolling bench. The final average size of BFO HNPs suspended in ethanol is approximately 140 nm as estimated from dynamic light scattering (DLS, Fig.S.I.1).[20]

Synthesis of Lanthanide Upconversion Nanoparticles $NaGdF_4$: 20% Yb^{3+}/2% Er^{3+} (Ln-UCNPs) A previously reported thermal decomposition approach was used for

the synthesis of monodisperse upconverting $NaGdF_4$: 20% Yb^{3+}/2% Er^{3+}.[37] In brief, lanthanide precursors were prepared under reflux (80° C) by mixing of Yb_2O_3 (2.5×10^{-04} mole, 0.0985 g), Er_2O_3 (2.5×10^{-05} mole, 0.0096 g), and Gd_2O_3 (9.75×10^{-04} mole, 0.534 g) with 5 mL distilled water and 5 mL trifluoroacetic acid for 12 hours. The transparent liquid precursors were air dried at 60° C for 16 hours, forming a white solid powder. Dried precursors were heated to 125° C in the presence of 7.5 mL 1-octadecene, 7.5 mL oleic acid, and sodium trifluoroacetate (2.5×10^{-03} mole, 0.34 g). Simultaneously, in a three neck 100 mL flask (receiving flask), 12.5 mL 1-octadecene, and 12.5 mL oleic acid were heated under vacuum to 150° C for a period of 30 minutes. The temperature of the receiving flask was increased to 310° C, under an inert atmosphere (argon), followed by the injection of the precursor using a syringe pump system at a rate of 1.5 mL/min. The reaction mixture was stirred for 60 minutes after which the solution was cooled down to room temperature. 100 mL of absolute ethanol was added to the solution, and the nanoparticles were precipitated by centrifugation at 3400 rpm for 15 minutes. The precipitate was washed twice using a hexane/ethanol (1:4) mixture.

Silica Coated $NaGdF_4$: 20% Yb^{3+}/2% Er^{3+} The $NaGdF_4$: 20% Yb^{3+}/2% Er^{3+} nanoparticles are oleate capped, and dispersible in non-polar organic solvents. A silica shell was added to render nanoparticles water dispersible using a water-in-oil reverse microemulsion method.[38] First, 20 mg of the oleate capped $NaGdF_4$: 20% Yb^{3+}/2% Er^{3+} nanoparticles were dispersed in cyclohexane (10 mL) and sonicated for 10 minutes. The non-ionic surfactant Igepal CO-520 (Octylphenoxy poly(ethyleneoxy)ethanol) (0.1 mL) was added to the nanoparticles under sonication for 10 minutes, and the mixture stirred at 600 rpm for 20 minutes. Another two portions of 0.4 mL Igepal CO-520 were added with 10 minutes interval between each portion. Ammonium hydroxide (80 μL, 28%) was added to the solution followed by sonication until solution becomes clear. 20 μL of tetraethyl orthosilicate (TEOS) were added to the reaction mixture, and stirred for 48 hours. For purification, 20 mL of

acetone was added to the mixture followed by centrifugation at 3400 rpm. The precipitate was washed twice using an ethanol-water (1:1) mixture, and the nanoparticles were stored in the same solution.

Laser Irradiation Parameters The measurements were performed with a Mai-Tai or altenatively an Insight tunable laser (Newport Spectra-Physics) at 80 MHz repetition rate. The pulse duration at the sample after transmission through the microscope optics and the air objective (Plan APO 20× WI N.A. 0.75) is $t_{pulse} = 190$ fs at FWHM.

Assuminga spatial Gaussian profile of focal diameter $\frac{\lambda}{2\mathrm{NA}}$, the peak irradiance (or peak intensity) is calculated at FWHM of the laser temporal and spatial profile as[24]

$$I_{peak} = \frac{16 P_{av} \mathrm{NA}^2}{R t_{pulse} \pi \lambda^2}$$

where P_{av} is the average incident power and R the laser repetition rate.

Pulse density is defined for a specific scan as

$$d_{pulse} = \frac{R}{v\, P_{size}} = \frac{R \times t_d}{P_{size}^2}$$

where v is the scanning speed of the laser focal spot, P_{size} the lateral pixel dimension, and t_d the dwell time.

The corresponding irradiation dose associated with a single image frame is

$$F_{total} = d_{pulse} \times E_{pulse}$$

where E_{pulse} is the pulse energy.

Cells and Cell Co-Cultures For the measurements in Fig. 1, we used Red Fluorescent Protein (RFP) expressing adenocarcinomic human alveolar basal epithelial cells A549.

For the co-culture measurements (Fig. 4 and S.I. 4), wild-type A549 and cells preloaded

of BFO HNPs by g-force method were co-cultured by simultaneous plating on glass-bottom dishes (35 mm Glass Bottom Dishes, No 1.5 Uncoated, MatTek Corporation). The co-culture was suspended in a total of 2 mL cell culture medium. Cells were allowed to adhere for 24 hours before imaging. The co-culture plated on a 20 mm diameter glass bottom dish contained 10^3 A549 cells pre-loaded with BFO and 10^5 non-labeled A549, yielding a ratio of 1:100. The number of cells was determined using a hemocytometer.

***g*-Force Induced Internalization of BFO into Cells** To internalize BFO nanoparticles into cells used for co-cultures, the g-force based delivery method was used.[39] Briefly, adherent A549 cells were detached by incubation for 5 minutes in trypsin/EDTA (Ethylenediaminetetraacetic acid) 0.25% solution diluted in DPBS (Dulbecco's phosphate-buffered saline). After removing trypsin using centrifugation precipitation of cells, the cell pellet was resuspended in 1 mL of cellular media with a final cellular count of 10^6 cells. BFO nanoparticles were pre-sonicated for 30 min in PBS buffer and added to the cellular suspension at a final concentration 0.2 mg/mL. After gentle vortex, cell suspension was centrifuged for 5 minutes at 400 g (MiniSpin plus, Vaudaux-Eppendorf AG . Next, the cells were resuspended and plated for culturing. For further use and imaging BFO preloaded cells were treated using the same protocols as for normal cells.

For the assessment in Fig. 1, the internalization of nanoparticles relied on overnight incubation of RFP expressing A549 cells with BFO in medium at 100 μg/mL concentration. The cells were rinsed three times in PBS before performing the experiment.

Hyperspectral Imaging Hyperspectral imaging was performed using a Nikon multiphoton inverted microscope (A1R-MP) coupled with a Mai-Tai tunable Ti:sapphire oscillator from Spectra-Physics (100 fs, 80 MHz, 700–1000 nm). A Plan APO 20× WI N.A. 0.75 objective was used to focus the excitation laser and to epi-collect the SHG signal. The signal was collected and directed through an optical fiber to the spectral detector, where it was diffracted by a grating and projected on a 32-PMT array. Cellular autofluorescence was

induced at 720 nm and SHG was excited at 980 nm. Spectra were acquired in the range 400 nm to 650 nm and the resolution was set to 10 nm. Live cell imaging was performed at 37° C using Okolab incubator (Pozzuoli, NA, Italy) with humidity and CO_2 control.

Determination of Damage Thresholds To determine the damage thresholds of i) BFO HNPs, ii) unlabelled cells, and iii) labelled cells, we performed measurements under different scanning and laser conditions.

i) The sample was prepared by casting a drop of BFO HNPs suspended in ethanol on a microscope cover-slip and letting the solvent evaporate. An irradiation was arbitrarily labelled as unsafe (red stars) if during the first image frame we observed a drop of more than 10% of the signal from the particle ensemble and if after 100 successive frames the signal decreased by more than 20% with respect to the initial value, safe (green stars) otherwise.

ii and iii) We measured RFP expressing live cells plated on a Petri dish not at confluence both unlabelled and with internalized BFO HNPs. An irradiation was considered unsafe (red circles) if we observed the sudden appearance of one or multiple hyperfluorescence spots during the first frame, successively developing as larger bright rings during the successive frames, eventually leaving a dark region in the middle.

The relevant scanning characteristics (dwell time, pixel size, scanning speed) to determine d_{pulse} and other excitation parameters were obtained directly from the microscope software interface (Nikon Elements).

Nanothermometry Nanothermometric imaging was performed on BFO nanoparticles dried together with upconverting nanoparticles (UCNPs) $NaGdF_4$: Yb^{3+}/Er^{3+} with an average size of 36 nm coated with Silica shell of 2 nm. Imaging was performed using 980 nm at 0.85 TW/cm^2. Emission of harmonic and upconverting nanoparticles was recorded using hyperspectral detection. The fluorescence response of UCNPs was converted to temperature change based on a calibration obtained from imaging dried UCNPs at different temperatures. For this experiment, UCNPs at 5 mg/ml were dried on a glass coverslip and the

sample was deposited under using a home-built Peltier element based thermostat. Acquired fluorescence of UCNPs was spectrally unmixed using UCNPs 520 nm (510-535 nm) and 540 nm(535-565 nm) bands as reference spectra. Unmixed images were used for the construction of ratiometric images. Images of HNPs mixed with UCNPs samples were acquired and also spectrally unmixed.

For the experiment in cell medium, UCNPs were suspended at final concentration of 100 μg/ml. An aliquot of presonicated BFO HNPs was added to the solution to obtain 50 μg/ml concentration. Before measurements, samples were let on the microscope stage for 25 minutes to allow NPs to precipitate. Imaging and temperature quantification were performed following the same protocol as for dry nanoparticles.

Acknowledgements

The authors acknowledge support from the Swiss National Science Foundation through the NCCR MUST (Molecular Ultrafast Science and Technology) Network. J. A. C. is a Concordia University Research Chair in Nanoscience and is grateful to Concordia University for financial support. J. A. C. is grateful to the Natural Science and Engineering Research Council (NSERC) of Canada for the sustained support of his research. Y.M, C.M., and L.B acknowledge the support of the France-Switzerland Programme Interreg. We are thankful to M. Moret, engineer at Department of Applied Physics, for the technical support in setting-up the experiment.

Authors' contributions

V. K. designed the experiment and performed the optical measurements. G.C., I. F., S. S., A.C., F. R., Y. M. performed selected optical and XRD measurements. T. S. and J. C. defined the UCNPs synthesis protocol and produced the UCNPs particles. V. K, I. F., D. S., C. M. prepared the samples. V. K. and G. C. analyzed the data. V. K., J. A. C, J.-P. W.

designed the experiment. V. K., L. B., and A.V wrote the manuscript. All authors helped in the data interpretation and critically read and approved the manuscript.

Supporting Information

The Supporting Information is available free of charge at: https://... Supplemental information include: size distribution of BFO HNPs, emission spectra of BFO HNPs at different irradiations, evolution of SHG signal upon irradiation, *In Situ* characterization of the temperature increase around a BFO HNPs in cell medium, XRD pattern of BFO HNPs upon different irradiation conditions, hyperspectral images of cell co-cultures.

References

1. Riley, R. S.; Day, E. S. Gold Nanoparticle-Mediated Photothermal Therapy: Applications and Opportunities for Multimodal Cancer Treatment. *Wiley Interdiscip. Rev. Nanomed. Nanobiotechnol.* **2017**, *9*, e1449.

2. Dubreil, L.; Leroux, I.; Ledevin, M.; Schleder, C.; Lagalice, L.; Lovo, C.; Fleurisson, R.; Passemard, S.; Kilin, V.; Gerber-Lemaire, S.; Colle, M.-A.; Bonacina, L.; Rouger, K. Multi-Harmonic Imaging in the Second Near-Infrared Window of Nanoparticle-Labeled Stem Cells as Monitoring Tool in Tissue Depth. *ACS Nano* **2017**, *11*, 6672–6681.

3. Ramos-Gomes, F.; Möbius, W.; Bonacina, L.; Alves, F.; Markus, M. A. Bismuth Ferrite Second Harmonic Nanoparticles for Pulmonary Macrophage Tracking. *Small* **2019**, *15*, 1803776.

4. Débarre, D.; Pena, A. M.; Supatto, W.; Boulesteix, T.; Strupler, M.; Sauviat, M. P.; Martin, J. L.; Schanne-Klein, M. C.; Beaurepaire, E. Second- and Third-Harmonic Generation Microscopies for the Structural Imaging of Intact Tissues. *M S - Med. Sci.* **2006**, *22*, 845–850.

5. Riporto, J.; Urbain, M.; Mugnier, Y.; Multian, V.; Riporto, F.; Bredillet, K.; Beauquis, S.; Galez, C.; Monnier, V.; Chevolot, Y. Second Harmonic Spectroscopy of ZnO, BiFeO 3 and $LiNbO_3$3 Nanocrystals. *Opt. Mater. Express* **2019**, *9*, 1955–1966.

6. Urban, B. E.; Neogi, P. B.; Butler, S. J.; Fujita, Y.; Neogi, A. Second Harmonic Imaging of Plants Tissues and Cell Implosion Using Two-Photon Process in ZnO Nanoparticles. *J. Biophotonics* **2012**, *5*, 283–291.

7. Voss, T.; Kudyk, I.; Wischmeier, L.; Gutowski, J. Nonlinear Optics with ZnO Nanowires. *Phys. Status Solidi* **2009**, *246*, 311–314.

8. Vogel, A.; Noack, J.; Hüttman, G.; Paltauf, G. Mechanisms of Femtosecond Laser Nanosurgery of Cells and Tissues. *Appl. Phys. B* **2005**, *81*, 1015–1047.

9. Nagy, B.; Gallais, L.; Vámos, L.; Oszetzky, D.; Rácz, P.; Dombi, P. Direct Comparison of Kilohertz-and Megahertz-Repetition-Rate Femtosecond Damage Threshold. *Opt. Lett.* **2015**, *40*, 2525–2528.

10. Kumar, A.; Rai, R. C.; Podraza, N. J.; Denev, S.; Ramirez, M.; Chu, Y.-H.; Martin, L. W.; Ihlefeld, J.; Heeg, T.; Schubert, J. Linear and Nonlinear Optical Properties of $BiFeO_3$3. *Appl. Phys. Lett.* **2008**, *92*, 121915.

11. Lin, J.; Fujita, Y.; Neogi, A. Saturation of Two Photon Emission in ZnO Nanoparticles with Second Order Nonlinearity. *RSC Adv.* **2015**, *5*, 10921–10926.

12. Soram, B. S.; Ngangom, B. S.; Sharma, H. B. Effect of Annealing Temperatures on the Structural and Optical Properties of Sol–Gel Processed Nanocrystalline BiFeO3 Thin Films. *Thin Solid Films* **2012**, *524*, 57–61.

13. Boyd, R. W. *Nonlinear Optics 3d Ed.*; Academic Press, Cambridge (Massachusetts), 2008, 33-58.

14. Rojac, T.; Bencan, A.; Malic, B.; Tutuncu, G.; Jones, J. L.; Daniels, J. E.; Damjanovic, D. $BiFeO_3$ Ceramics: Processing, Electrical, and Electromechanical Properties. *J. Am. Ceram. Soc.* **2014**, *97*, 1993–2011.

15. Kirsch, A.; Murshed, M. M.; Litterst, F. J.; Gesing, T. M. Structural, Spectroscopic, and Thermoanalytic Studies on Bi2Fe4O9: Tunable Properties Driven by Nano- and Poly-Crystalline States. *J. Phys. Chem. C* **2019**, *123*, 3161–3171.

16. Ichimura, N.; Kondo, H.; Harada, Y.; Hashimoto, S. Formation of High Density Color Centers and Laser Ablation in Alkali Halide Crystals. *J. Lumin.* **2000**, *87*, 586–588.

17. Gaudiuso, C.; Giannuzzi, G.; Volpe, A.; Lugarà, P. M.; Choquet, I.; Ancona, A. Incubation during Laser Ablation with Bursts of Femtosecond Pulses with Picosecond Delays. *Opt. Express* **2018**, *26*, 3801–3813.

18. Vetrone, F.; Naccache, R.; Zamarron, A.; Juarranz de la Fuente, A.; Sanz-Rodríguez, F.; Martinez Maestro, L.; Martín Rodriguez, E.; Jaque, D.; García Solé, J.; Capobianco, J. A. Temperature Sensing Using Fluorescent Nanothermometers. *ACS Nano* **2010**, *4*, 3254–3258.

19. Quintanilla, M.; Zhang, Y.; Liz-Marzán, L. M. Subtissue Plasmonic Heating Monitored with CaF_2: N^{3+}, Y^{3+} Nanothermometers in the Second Biological Window. *Chem. Mat.* **2018**, *30*, 2819–2828.

20. Schwung, S.; Rogov, A.; Clarke, G.; Joulaud, C.; Magouroux, T.; Staedler, D.; Passemard, S.; Justel, T.; Badie, L.; Galez, C. Nonlinear Optical and Magnetic Properties of $BiFeO_3$ Harmonic Nanoparticles. *J. of Appl. Phys.* **2014**, *116*, 114306.

21. Balabhadra, S.; Debasu, M. L.; Brites, C. D. S.; Ferreira, R. A. S.; Carlos, L. D. Upconverting Nanoparticles Working as Primary Thermometers in Different Media. *J. Phys. Chem. C* **2017**, *121*, 13962–13968.

22. Quintanilla, M.; Garcia, I.; de Lazaro, I.; Garcia-Alvarez, R.; Henriksen-Lacey, M.; Vranic, S.; Kostarelos, K.; Liz-Marzan, L. M. Thermal Monitoring during Photothermia: Hybrid Probes for Simultaneous Plasmonic Heating and Near-Infrared Optical Nanothermometry. *Theranostics* **2019**, *9*, 7298–7312.

23. König, K.; Becker, T.; Fischer, P.; Riemann, I.; Halbhuber, K.-J. Pulse-Length Dependence of Cellular Response to Intense Near-Infrared Laser Pulses in Multiphoton Microscopes. *Opt. Lett.* **1999**, *24*, 113–115.

24. Supatto, W.; Débarre, D.; Farge, E.; Beaurepaire, E. Femtosecond Pulse-Induced Microprocessing of Live Drosophila Embryos. *Med. Laser Appl.* **2005**, *20*, 207–216.

25. Orzekowsky-Schroeder, R.; Klinger, A.; Martensen, B.; Blessenohl, M.; Gebert, A.; Vogel, A.; Huttmann, G. *In Vivo* Spectral Imaging of Different Cell Types in the Small Intestine by Two-Photon Excited Autofluorescence. *J. Biomed. Opt.* **2011**, *16*, 116025.

26. Kuetemeyer, K.; Rezgui, R.; Lubatschowski, H.; Heisterkamp, A. Influence of Laser Parameters and Staining on Femtosecond Laser-Based Intracellular Nanosurgery. *Biomed. Opt. Express* **2010**, *1*, 587–597.

27. Qin, Z.; Sun, Q.; Lin, Y.; He, S.; Li, X.; Chen, C.; Wu, W.; Luo, Y.; Qu, J. Y. New Fluorescent Compounds Produced by Femtosecond Laser Surgery in Biological Tissues: The Mechanisms. *Biomed. Opt. Express* **2018**, *9*, 3373–3390.

28. Sun, Q.; Qin, Z.; Wu, W.; Lin, Y.; Chen, C.; He, S.; Li, X.; Wu, Z.; Luo, Y.; Qu, J. Y. *In Vivo* Imaging-Guided Microsurgery Based on Femtosecond Laser Produced New Fluorescent Compounds in Biological Tissues. *Biomed. Opt. Express* **2018**, *9*, 581–590.

29. Hovhannisyan, V.; Lo, W.; Hu, C.; Chen, S.-J.; Dong, C. Y. Dynamics of Femtosecond Laser Photo-Modification of Collagen Fibers. *Opt. Express* **2008**, *16*, 7958–7968.

30. Liang, X.-X.; Zhang, Z.; Vogel, A. Multi-Rate-Equation Modeling of the Energy Spectrum of Laser-Induced Conduction Band Electronsin Water. *Opt. Express* **2019**, *27*, 4672–4693.

31. Lee, H.; Alt, C.; Pitsillides, C. M.; Lin, C. P. Optical Detection of Intracellular Cavitation during Selective Laser Targeting of the Retinal Pigment Epithelium: Dependence of Cell Death Mechanism on Pulse Duration. *J. Biomed. Opt.* **2007**, *12*, 064034.

32. Simanovskii, D. M.; Mackanos, M. A.; Irani, A. R.; O'Connell-Rodwell, C. E.; Contag, C. H.; Schwettman, H. A.; Palanker, D. V. Cellular Tolerance to Pulsed Hyperthermia. *Phys. Rev. E* **2006**, *74*, 011915.

33. Abadeer, N. S.; Murphy, C. J. Recent Progress in Cancer Thermal Therapy Using Gold Nanoparticles. *J. Phys. Chem. C* **2016**, *120*, 4691–4716.

34. Sordillo, L. A.; Pu, Y.; Pratavieira, S.; Budansky, Y.; Alfano, R. R. Deep Optical Imaging of Tissue Using the Second and Third Near-Infrared Spectral Windows. *J. Biomed. Opt.* **2014**, *19*, 056004–056004.

35. Harmsen, S.; Teraphongphom, N.; Tweedle, M. F.; Basilion, J. P.; Rosenthal, E. L. Optical Surgical Navigation for Precision in Tumor Resections. *Mol. Imaging Biol.* **2017**, *19*, 357–362.

36. Lukic, A.; Dochow, S.; Bae, H.; Matz, G.; Latka, I.; Messerschmidt, B.; Schmitt, M.; Popp, J. Endoscopic Fiber Probe for Nonlinear Spectroscopic Imaging. *Optica* **2017**, *4*, 496–501.

37. Sabri, T.; Pawelek, P. D.; Capobianco, J. A., Dual Activity of Rose Bengal Functionalized to Albumin-Coated Lanthanide-Doped Upconverting Nanoparticles: Targeting and Photodynamic Therapy. *ACS Appl. Mat. Interfaces* **2018**, *10*, 26947–26953.

38. Kostiv, U.; Janoušková, O.; Šlouf, M.; Kotov, N.; Engstová, H.; Smolková, K.; Ježek, P.; Horák, D. J. N. Silica-Modified Monodisperse Hexagonal Lanthanide Nanocrystals: Synthesis and Biological Properties. *Nanoscale* **2015**, *7*, 18096–18104.

39. Ocampo, S. M.; Rodriguez, V.; De La Cueva, L.; Salas, G.; Carrascosa, J. L.; Rodríguez, M. J.; García-Romero, N.; Cuñado, J. L. F.; Camarero, J.; Miranda, R. G-Force Induced Giant Efficiency of Nanoparticles Internalization into Living Cells. *Sci. Rep.* **2015**, *5*, 15160.